

Spin exchange Hamiltonian and topological degeneracies in elemental gadolinium

A. Scheie,^{1,*} Pontus Laurell,^{2,3} G. E. Granroth,¹ M. B. Stone,¹ and S. E. Nagler^{1,4}

¹Neutron Scattering Division, Oak Ridge National Laboratory, Oak Ridge, TN 37831, USA

²Computational Sciences and Engineering Division, Oak Ridge National Laboratory, Oak Ridge, TN 37831, USA

³Department of Physics and Astronomy, University of Tennessee, Knoxville, TN 37996, USA.

⁴Quantum Science Center, Oak Ridge National Laboratory, Tennessee 37831, USA

(Dated: September 11, 2022)

We present a comprehensive study of the magnetic exchange Hamiltonian of elemental Gadolinium. We use neutron scattering to measure the magnon spectrum over the entire Brillouin zone, and fit the excitations to a spin wave model to extract the first 30 nearest neighbor magnetic exchange interactions with rigorously defined uncertainty. We find these exchange interactions to follow RKKY behavior, oscillating from ferromagnetic to antiferromagnetic as a function of distance. Finally, we discuss the topological features and degeneracies in Gd, and HCP ferromagnets in general. We show theoretically how, with asymmetric exchange, topological properties could be tuned with a magnetic field.

I. INTRODUCTION

Gadolinium (Gd) is one of the few elemental ferromagnets [1]. It is considered a “critical material” to industry because of its unique magnetic properties [2–4], and yet the mechanisms behind its magnetism are not fully understood. In this study, we use inelastic neutron scattering to determine the magnetic exchange Hamiltonian of elemental Gd to the 30th neighbor exchange, showing the exchange approximately follows an Ruderman-Kittel-Kasuya-Yoshida (RKKY) model. In a separate paper [5] we also show that these spin waves yield topological features; in this paper we extend this topology discussion with further details about anisotropic HCP rare earths.

The Gd crystal structure is hexagonal close packed (HCP), shown in Fig. 1. Elemental Gd orders ferromagnetically [1] with a Curie temperature $T_c = 293$ K [6, 7]. Its magnetism is almost perfectly isotropic: the first three valence electrons are itinerant, leaving an effective Gd^{3+} at each site [8] with a quenched orbital moment and well-defined $S = 7/2$ [9]. Small anisotropies do exist in Gd [10], which vary as a function of temperature [7, 11] and appear to be from interaction between the itinerant electrons and localized $4f$ electrons [12, 13].

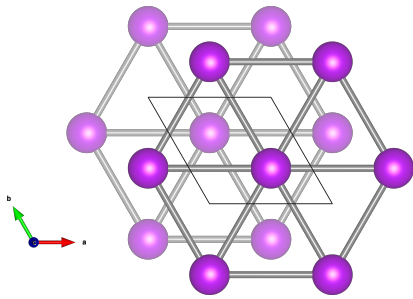


Figure 1. HCP crystal structure of Gd, with layers of triangular lattices.

The Gd inelastic neutron spectrum was first measured in 1970 [14], and it is a textbook example of ferromagnetic spin waves [15, 16]. However the original measurements, performed on a triple-axis spectrometer, were only along high-symmetry directions. This led to limitations in fitting a spin wave Hamiltonian [17]: in-plane and out-of-plane exchanges could not be fitted simultaneously. Fortunately, neutron spectrometers have dramatically improved over the last 50 years [18]. In this study, we measure the inelastic neutron spectrum of elemental Gd over the entire Brillouin zone using modern instrumentation. This allows us to rigorously fit the excitations to a full spin wave model, compare to RKKY exchange strengths, and observe topological features in the data.

This paper is organized as follows: section II explains the neutron scattering experiment on Gd, section III shows the spin wave fits to the scattering data and compares the exchanges to RKKY, and section IV discusses the topology of the Gd magnon band structure.

II. EXPERIMENT

We measured the spin waves of Gd using the SEQUOIA spectrometer [19, 20] at the ORNL SNS [21]. Because most Gd isotopes have an extremely high neutron absorption cross section, we measured a 12 g isotopically enriched ^{160}Gd single crystal (in fact, the same crystal as was used in Ref. [14]). The sample was mounted in the $(h\ell)$ plane in a closed cycle refrigerator, and cooled to 5 K. We measured the neutron spectrum at incident energies $E_i = 50$ meV and 100 meV. ($T0$ chopper at 90 Hz, Fermi 1 chopper at 120 Hz, Fermi 2 chopper at 360 Hz for $E_i = 50$ meV, slits 36 mm wide and 14 mm tall. For $E_i = 100$ meV the same chopper speeds were used but with the Fermi 2 chopper at 540 Hz.) We rotated the sample about the vertical axis in one degree steps over 180 degrees. Data were reduced and symmetrized [22] to fill out the full Brillouin zone. Measurements were performed with the SNS operating at 1.4 MW over the course of two days.

Some slices of the Gd scattering data are shown in Fig. 2(a)-(d) with constant Q cuts in Fig. 3; see the Supplemental Information [23] for more plots. The magnon modes are

* scheieao@ornl.gov

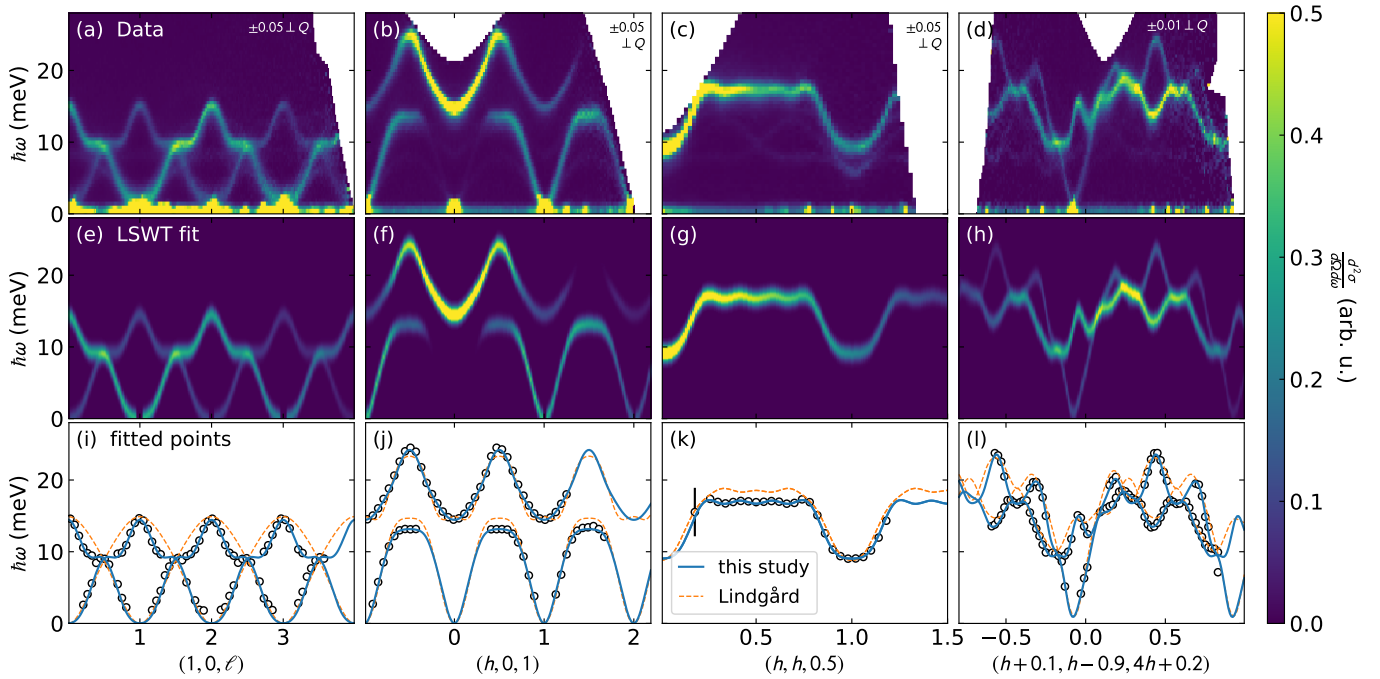


Figure 2. Measured and fitted spin wave spectra of Gd. The top row (a)-(d) shows the measured spin wave spectra of Gd. The Q width in the direction perpendicular to the x axis is shown in the upper right of each panel. The middle row (e)-(h) shows the LSWT calculated spectrum from the best fit Hamiltonian in Table I. The bottom row (i)-(l) shows a portion of the data points used in the fit (black circles), and the fitted dispersion from this study (blue solid line) and Lindgård [17] (orange dashed line).

sharp and well defined even at the top of the dispersion, which indicates localized moments as expected. Because of the large $S = 7/2$ spin, the magnon intensity is much larger than phonon intensity at 5 K for the measured wavevectors. The phonons look very similar to the magnons due to the HCP structure: in certain slices [like $(h, h, 0.5)$ in Fig. 2(c)], the phonon modes appear as faint modes at lower energies. However, the phonons can be distinguished by the fact that their intensity grows with momentum transfer $|Q|$, while the magnon intensity decreases.

III. SPIN WAVE FIT

To date, the most comprehensive Hamiltonian fit to Gd spin waves was performed by Lindgård in 1978 [17]. This analysis used the inelastic neutron scattering data collected by Koehler in 1970 [14]. Lindgård included 11 exchange parameters fitted to hk plane scattering, but fitted the ℓ direction separately to a $J(\mathbf{Q})$ model (effectively calculating Fourier components) rather than including it in the fit. With our data set, we are able to perform a full, comprehensive Hamiltonian fit to the data.

The magnon dispersion of a HCP Heisenberg ferromagnet described by $\mathcal{H} = \sum_{ij} J_{ij} \mathbf{S}_i \cdot \mathbf{S}_j$ is derived in Ref. [16]. Although the magnon bands appear gapless in our neutron data, magnetic torque measurements reveal the single-ion anisotropy of Gd to be $37 \mu\text{eV}$. To first order, this produces a linear offset of all dispersion bands [16] of $37 \mu\text{eV}$, and we

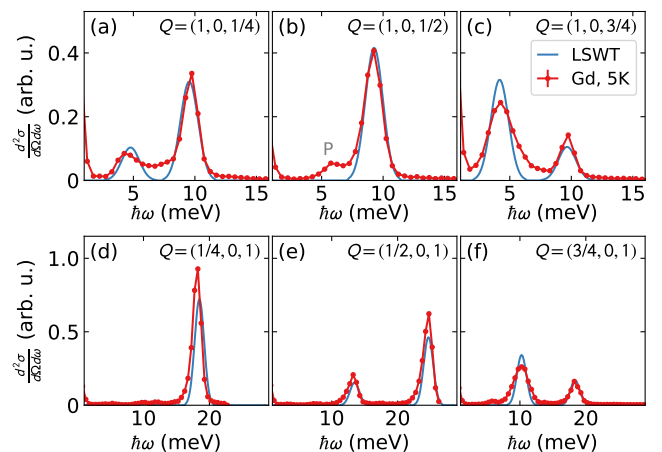


Figure 3. Constant Q cuts of Gd scattering along the $(1, 0, \ell)$ direction [top row, from Fig. 2(a)] and $(h, 0, 1)$ direction [bottom row, from Fig. 2(b)] compared to the best fit LSWT calculation. The magnon peaks are very clearly visible in the data. A phonon is visible in panel (b) at 6 meV, with much smaller intensity than the magnons. LSWT simulations have a energy peak full width half maximum of 1.5 meV, which roughly matches the experimental width at all energies.

incorporated this effect into our model. Beyond this single-ion anisotropy, we assumed that all exchanges are isotropic in accord with Gd's quenched orbital moment.

In order to fit the magnon dispersions to the observed en-

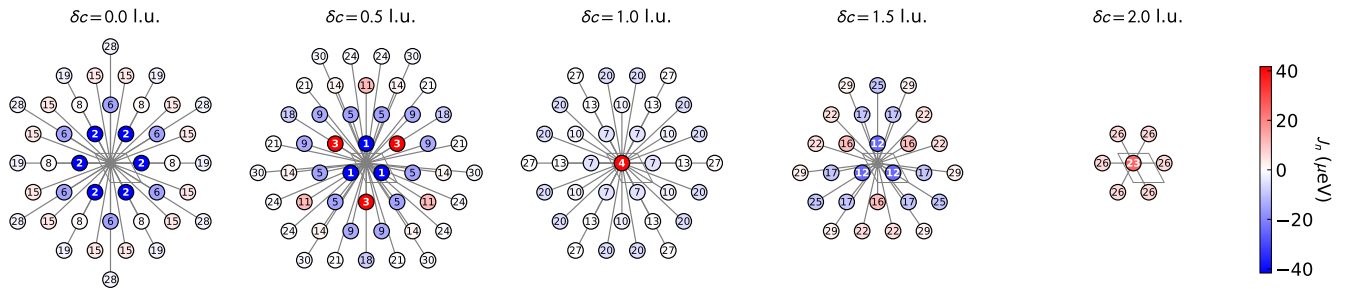


Figure 4. Neighbor bond length and magnitude of the refined exchange for Gd. The five panels indicate different layers along the c axis, where δc in each panel indicates the bond length along the c axis. The number in each circle denotes the neighbor number. The color indicates the fitted exchange interaction: ferromagnetic exchange is indicated by blue, antiferromagnetic by red, with the magnitude indicated by the color bar on the right.

Table I. Refined exchange constants for Gd, in units of μeV . Positive values indicate antiferromagnetic exchange, negative values indicate ferromagnetic exchange.

$J_1 = -133 \pm 9$	$J_{11} = 11 \pm 11$	$J_{21} = -0.5 \pm 0.4$
$J_2 = -174 \pm 3$	$J_{12} = -25 \pm 7$	$J_{22} = 5 \pm 4$
$J_3 = 44 \pm 11$	$J_{13} = -0.6 \pm 0.4$	$J_{23} = 25 \pm 4$
$J_4 = 40 \pm 4$	$J_{14} = 2 \pm 10$	$J_{24} = -1 \pm 3$
$J_5 = -20 \pm 20$	$J_{15} = 3.8 \pm 1.0$	$J_{25} = -9 \pm 5$
$J_6 = -15 \pm 2$	$J_{16} = 11 \pm 5$	$J_{26} = 6.1 \pm 1.4$
$J_7 = -4.6 \pm 0.8$	$J_{17} = -9 \pm 7$	$J_{27} = 0.5 \pm 0.3$
$J_8 = 0.8 \pm 0.5$	$J_{18} = -8 \pm 9$	$J_{28} = -1.67 \pm 0.12$
$J_9 = -14 \pm 11$	$J_{19} = -2 \pm 2$	$J_{29} = 2 \pm 5$
$J_{10} = -2.3 \pm 0.6$	$J_{20} = -5.3 \pm 0.4$	$J_{30} = -1 \pm 3$

ergies, we extracted the magnon dispersion from the data by fitting the magnon modes with Gaussian peaks as a function of energy transfer for fixed values of wave-vector. We used over 37 different \mathbf{Q} vs $\hbar\omega$ slices through our data (see Fig 2(i)-(l) for examples and the Supplemental Information [23] for a complete list), which yielded a total of 1622 unique \mathbf{Q} points. We found that including data away from high-symmetry directions was important for constraining the fit, hence the large number of slices. These mode energy points were used to define a global χ^2 .

To determine the exchange constant terms, we compared the analytical form of the dispersion [16] to the determined energy transfer of the 1622 unique wave-vectors including an overall offset of 0.037 meV to account for the anisotropy as described earlier. The fitting procedure itself involved a stochastic simulated annealing method based on Scipy's minimization package [24] and is described in detail in Appendix A. We found that at least 26 nearest neighbors are required to accurately describe the details of the Gd magnon modes, and in our fit we kept up to the 30 nearest neighbors. The best fit parameters with uncertainty are shown in Table I, and are visually depicted in Fig. 4. The simulated neutron spectrum is plotted in Fig. 2(e)-(h). In every cut, the simulation matches the data quite well.

We examined χ^2 as a function of neighbors included in the

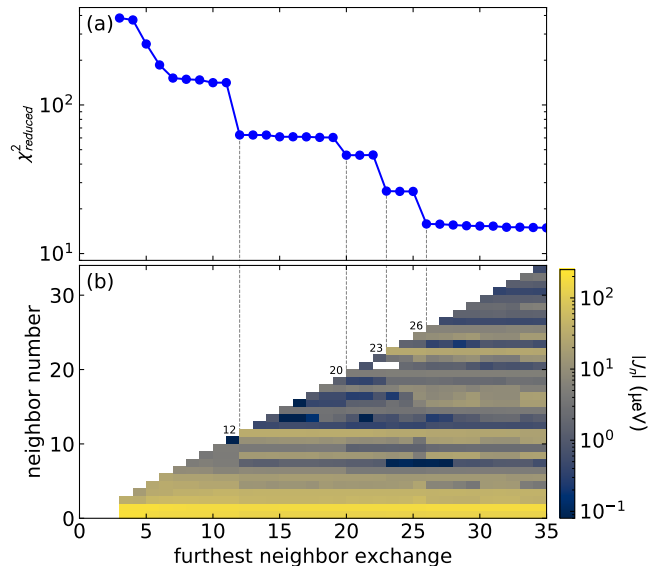


Figure 5. Fit vs number of fitted parameters. Panel (a) shows the χ^2_{reduced} as a function of number of parameters. Panel (b) shows the absolute value of the fitted exchange constants. Note that a sudden drop in χ^2_{reduced} (seen at $n = 12, 20, 23,$ and 26) corresponds to a well-constrained parameter. Because χ^2_{reduced} only slowly decreases beyond $n = 26$, we cut off the fit at $n = 30$.

model, as shown in Fig. 5. We find that exchanges up to the 26th neighbor have a significant effect on the fit. By comparing Fig. 5 with Fig. 4, one can see that the drops in χ^2 correspond to either crossing additional lattice planes as terms are added to the Hamiltonian (neighbor $n = 12, 23$) or when exchanges in a particular direction not represented before are included in the Hamiltonian ($n = 20, 26$). Including exchanges up to 35th neighbor continues to improve the fit, though only slightly [Fig. 5(a)]. In our model, we ignored exchanges beyond the 30th nearest neighbor as insignificant within the uncertainty of our data.

We calculated the statistical uncertainty for these fitted parameters by computing the $\Delta\chi^2 = 1$ contour around the global minimum using a Monte Carlo Markov chain method. This gave a reliable estimate of statistical uncertainty, as well as

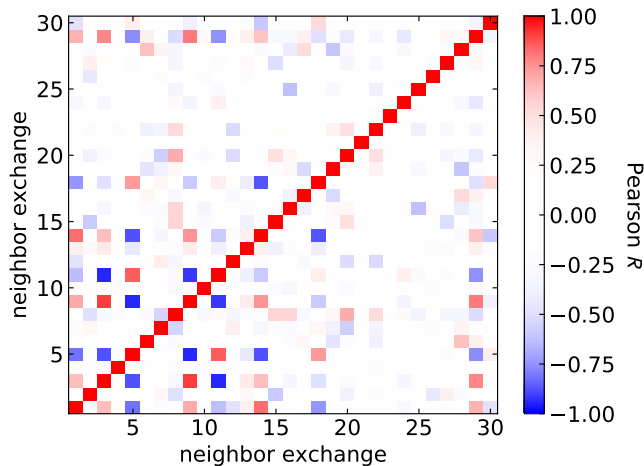


Figure 6. Correlation matrix for J_n from the Gd spin wave mode fits. Red indicates positive correlation, blue indicates negative correlation. Some parameters, like J_3 , are highly correlated with many other parameters. Others, like J_4 , have almost no correlation with other parameters, and thus are uniquely constrained by the data.

the correlation matrix between each parameter (visualized in Fig. 6). As is perhaps not surprising, many of the fitted exchange constants are highly correlated with one another. Indeed, principal component analysis reveals that 72.5% of the statistical variance of all exchange constants can be described by a single vector in $\{J_1, J_2, \dots, J_{30}\}$. Thus, the uncertainties in Table I are by no means independent: the parameters with the largest error bars are highly correlated with a set of other exchanges. In addition to this statistical uncertainty in the refined values, we also calculated the systematic uncertainty associated with truncating the Hamiltonian at the 30th nearest neighbor by taking the standard deviation of the parameters between $n_{max} = 30$ and $n_{max} = 35$ as the systematic uncertainty, which we added in quadrature with the statistical uncertainty to get the values in Table I.

We compare our refined Hamiltonian to the one proposed by Lindgård [17] in Fig 2(i)-(l). Lindgård's Hamiltonian has a reduced $\chi^2, \chi_{red}^2 = 442.1$ when compared to our data, whereas the Hamiltonian in Table I has $\chi_{red}^2 = 15.3$. This dramatic improvement is made possible by our much larger data set.

It is worth noting that the measurements in Ref. [14] were carried out at 78 K (compared to 5 K in our experiment). Subsequent measurements in the 1980's showed the Gd dispersion along c varies greatly between 9 K and 290 K [25–27], so some differences between the Lindgård Hamiltonian and our are expected. In general it appears that the higher frequency Q modulations in the modes vanish at higher temperatures, indicating that the exchange becomes more and more short-ranged as the temperature increases [26].

Comparison to RKKY

Despite the fact that Gd is ferromagnetic at low temperatures, many of the exchange constants are antiferromag-

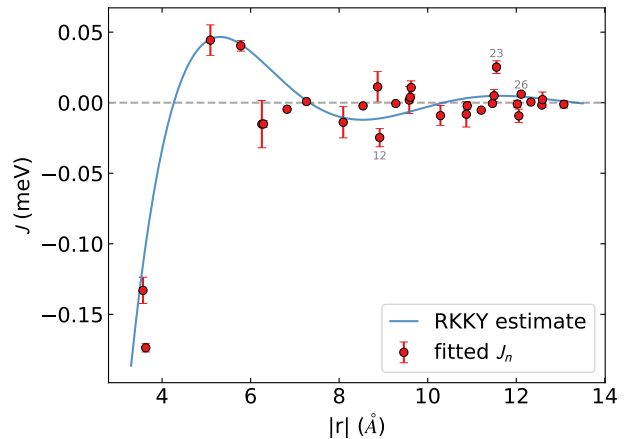


Figure 7. Refined values of magnetic exchange constants as a function of bond distance $|r|$ compared with a fitted RKKY exchange [Eq. (1)]. A few key points are labeled by their J_n index.

netic. Plotting the exchange constants against bond distance (Fig. 7) reveals an oscillation between ferromagnetism and antiferromagnetism as bond distance grows. This is consistent with Ruderman-Kittel-Kasuya-Yoshida (RKKY) exchange [28–30], where the magnetic exchange is mediated by conduction electrons.

The RKKY mechanism in three dimensions predicts a magnetic exchange Hamiltonian of the form

$$\mathcal{H} = A \mathbf{S}_i \cdot \mathbf{S}_j [2k_f r_{ij} \cos(2k_f r_{ij}) - \sin(2k_f r_{ij})] / r_{ij}^4, \quad (1)$$

[28] where k_f is the Fermi wavevector, r_{ij} is the bond distance, and A is a constant. The above equation assumes a spherical Fermi surface; because this is not quite true for Gd, we treat k_f in Eq. 1 as a fitted constant, fitting to the nearest 12 neighbors J_n where the oscillation is clearest. This yields $k_f = 0.53(2) \text{ \AA}^{-1}$ and the curve shown in Fig. 7. This fitted value is very close to the largest Fermi wavevectors measured by De Haas-Van Alphen oscillations (0.15 \AA^{-1} to 0.51 \AA^{-1}) [31], indicating that this the fitted k_f is reasonable and close to the actual Fermi surface radius. Of course, some of the fitted J_n do not follow the spherical RKKY model (most notably J_{23}), indicating non-sphericity of the Fermi surface or the presence of additional exchange mechanisms. Nevertheless, our results confirm that the RKKY mechanism is dominant in Gd. RKKY exchange has long been thought to be dominant in Gd [32–35], but here we show clear evidence in the exchange constants themselves.

IV. TOPOLOGY AND DEGENERACIES

Some features of the Gd spin wave spectrum do not depend on the fine details of the Hamiltonian: band degeneracies [36, 37] and associated topological invariants [38] are immune to perturbations of the exchange constants. As discussed in Ref. [5], the Gd neutron spectrum shows a nodal line degeneracy at $K = (1/3, 1/3, \ell)$ which has a π Berry phase around

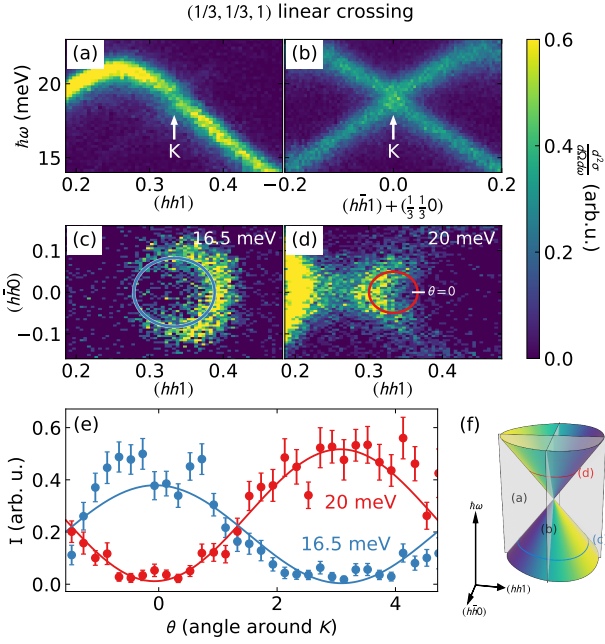


Figure 8. Linear band crossing at $K = (\frac{1}{3}, \frac{1}{3}, 1)$. Panels (a) and (b) show the measured neutron scattering for two orthogonal cuts through K , highlighting the anisotropic intensity around the dispersion cone. Panels (c) and (d) show constant energy slices above and below the band crossing, showing “intensity arcs”. Panel (e) shows the intensity binned around the circles in (c) and (d), fitted to a sin function. (f) The “Dirac node” dispersion surface, indicating the slices in panels (a)-(d), and with the color indicating the neutron scattering intensity.

it, and a nodal plane degeneracy at half-integer ℓ . An example of a K linear band crossing is shown in Fig. 8, which has the anisotropic winding intensity characteristic of non-trivial topology [39, 40]. These degeneracies are generic to all Heisenberg-only exchange Hamiltonians on the HCP lattice [36, 37], so long as the ferromagnetic ground state is preserved.

However, Gd is not the only elemental HCP ferromagnet. In materials with unquenched orbital momentum, the anisotropic Dzyaloshinskii-Moriya (DM) exchange interaction

$$H = \sum_{ij} \mathbf{D} \cdot (\mathbf{S}_i \times \mathbf{S}_j) \quad (2)$$

is expected, and it is interesting to consider the effects of other interactions on the band degeneracies and topology. Among the 30 nearest HCP neighbors, DM exchange is symmetry-allowed on the 2nd, 7th, 8th, 10th, 13th, 15th, 19th, 20th, 26th, and 27th neighbors [41]. Each DM exchange has a similar effect on the magnon degeneracies: nonzero DM exchange will tend to lift the degeneracy at the K point $(\frac{1}{3}, \frac{1}{3}, 0)$, as well as for most of the nodal plane, as shown in Fig. 9—although the splitting does depend upon the spin polarization direction. No gap at the Γ point $(0, 0, 0)$ is produced by DM exchange on the HCP lattice. However, a nodal line degeneracy along $A \rightarrow L$ is preserved even with nonzero asymmetric exchange, as shown in Fig. 9. This means that asymmetric exchange

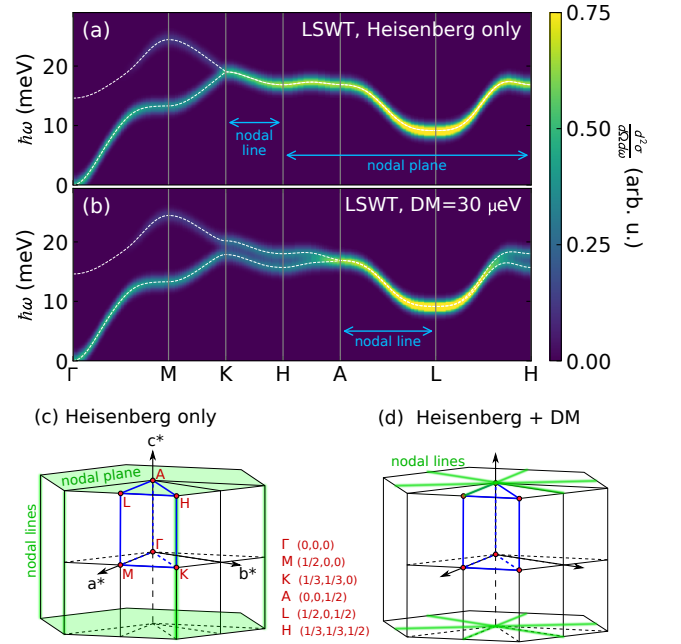


Figure 9. LSWT calculated spectrum along high symmetry directions without (a) and with (b) nonzero DM exchange interaction term on the second neighbor site. When $DM = 0$, K has a linear band crossing and all $\ell = 1/2$ is a nodal plane. When $DM > 0$, the $K \rightarrow H$ nodal line and the nodal plane degeneracies are broken, leaving nodal lines only along $A \rightarrow L$. Panel (c) shows the Brillouin zone nodal lines in (a), and panel (d) shows the same for (b).

leaves a triangular grid of $\ell = 1/2$ nodal lines in place of the nodal plane. In Gd, no mode splitting is resolvable, giving an upper bound of $3(1) \mu\text{eV}$ on the total asymmetric DM exchange in Gd (see Appendix B).

Intriguingly, the mode splitting at a given DM exchange strength can be tuned by changing the spin orientation. Because the 2nd neighbor DM vector (presumably the strongest asymmetric exchange) is constrained to point along the c -axis, when spins are polarized in the ab plane the mode splitting vanishes. Meanwhile, the mode splitting is maximal when spins are polarized along c . (Fig. 9 was calculated using the low-temperature Gd spin orientation; mode splitting with other spin orientations is explored in Fig. 10.) Thus, in the anisotropic HCP rare earths, it is in principle possible to tune the topological features by polarizing the spins along certain directions. By polarizing the spins in-plane, even highly anisotropic HCP magnets can be made to have nodal lines and planes like Gd.

The physical consequences of the nodal plane and the $\ell = 1/2$ nodal line grid have yet to be fully explored, but we can draw conclusions about the best understood feature: the nodal line Dirac cone at K . One of the reasons that Dirac magnons are of interest is because when symmetry is broken by DM exchange, chiral surface magnons are induced [38]. To explore this in the HCP context, we calculated the magnons for a 20 unit cell layer supercell HCP ferromagnet using SpinW [42], shown in Fig. 10. Using a simplified three-neighbor exchange

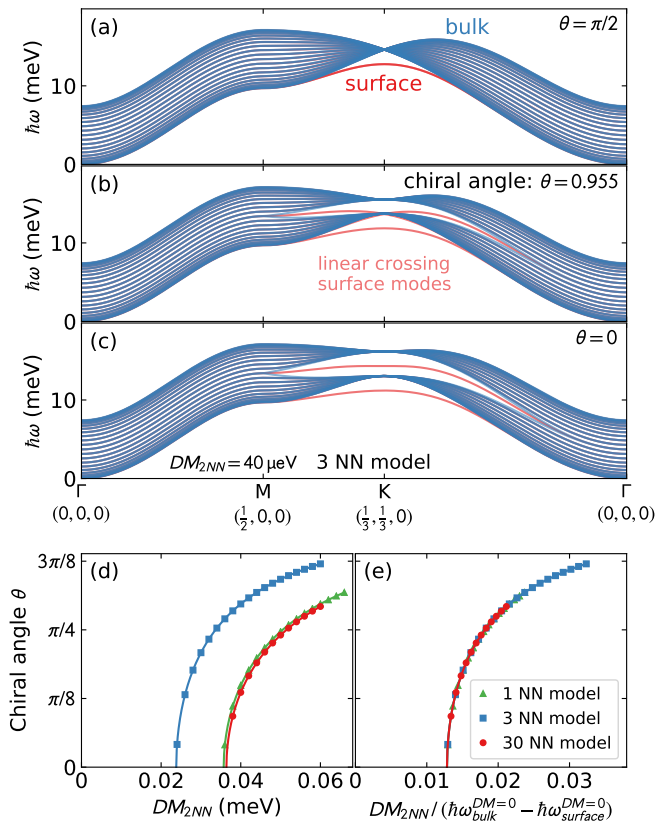


Figure 10. Chiral surface mode in the HCP ferromagnet. The top three panels show the bulk (periodic boundary conditions) and surface (c -axis termination) modes in a simplified 3 nearest neighbor (3NN) exchange model with a 2nd neighbor DM exchange of $40 \mu\text{eV}$. The three panels show the spins polarized at different angles θ from the c axis. The different spin polarizations induce different mode splitting because of the DM asymmetry. At a certain polarization angle, the two surface modes meet and cross with opposite slope, evidencing chiral surface magnon modes. For the simplified 3NN model, the chiral angle is $\theta = 0.955$. Panel (d) shows this chiral angle as a function of DM strength for different models: nearest neighbor exchange only (green), 3NN model (blue), and the full 30 neighbor model (red). In each case, a minimum DM exchange strength is necessary to produce the chiral mode crossing. Panel (e) shows these chiral angle is governed by the energy gap between the surface and bulk modes at K .

model, we calculated the modes both with periodic boundary conditions (shown in blue) and a c -axis termination simulated with a blank space at the top of the supercell (shown in red) with a second-neighbor DM exchange of $40 \mu\text{eV}$. The surface modes are clearly visible as lying outside the continuum of magnon states between $\ell = 0$ and $\ell = 1$.

As noted above, the DM magnon mode splitting can be tuned by the spin polarization angle from the c -axis. The calculations in Fig. 10(c)-(e) show that at a particular spin polarization angle, the surface magnon modes appear to cross at K with opposite velocities—potentially indicating chiral edge modes [38]. The specific angle depends upon the DM exchange interaction strength—but if DM exchange is strong enough, the system could host chiral edge states at that special

polarization angle.

This “chiral angle” is in fact a robust feature of HCP ferromagnets: we also calculated the surface magnons for the full 30-neighbor Gd exchange model with an added second-neighbor DM exchange, and found that—just like in the simplified model above—a linear surface-mode crossing was again induced at a particular spin-polarization angle from the c -axis [10(d)]. For all models, the chiral angle depends on DM interaction strength as $\arccos(C/DM)$ where C is a constant dependent upon the energy gap between the $DM = 0$ surface and bulk magnons at K . If we scale the chiral angle curve by the surface-bulk gap, the curves of various models collapse onto the same curve [10(e)]. The $\arccos(C/DM)$ dependence also gives a minimum threshold value for DM exchange, which depends upon the rest of the exchange Hamiltonian.

Besides Gd, some other elemental HCP ferromagnets are dysprosium [17, 43], terbium [17, 44], and hexagonal (α) cobalt [45]. Unlike Gd, these materials have unquenched orbital angular momentum and asymmetric exchange. Nodal plane splitting was actually measured in Tb [16, 44] to be $\sim 0.4 \text{ meV}$ —although the Tb spins being aligned in-plane [46] would tend to suppress mode splitting from DM, and other forms of anisotropy could be contributing to the mode splitting, rendering the actual DM strength uncertain. Be that as it may, Tb spin reorientation can be accomplished by a relatively modest $< 5 \text{ T}$ magnetic field [47], which suggests the possibility of tunable topology. It remains to be seen whether the anisotropic HCP rare earths have sufficiently strong asymmetric DM exchange for chiral edge modes discussed above—but if so this would mean that a magnetic field could switch on and off topological chiral magnon states.

V. CONCLUSION

We have measured the magnetic spectrum of elemental Gd over the entire Brillouin zone. We fit its magnetic exchange Hamiltonian to the 30th nearest neighbor, finding that the exchange interactions approximately follow an RKKY oscillation, in good agreement with long-standing expectations that RKKY exchange is relevant to Gd. We have also explored the topology and degeneracies of Gd, using that to predict the nodal lines of anisotropic HCP ferromagnets. Finally, we have used linear spin wave simulations to suggest how tunable topology may be induced in HCP ferromagnets with DM exchange.

These results showcase the ability of modern inelastic neutron spectrometers to precisely determine the magnetic exchange interactions with rigorous uncertainty. They also reveal the magnetic behavior of an industry-critical material, providing quantities to test against future theoretical studies. Perhaps most importantly, these results show the class of HCP magnets to be a useful platform for topological magnetism.

ACKNOWLEDGMENTS

This research used resources at the Spallation Neutron Source, a DOE Office of Science User Facility operated by the Oak Ridge National Laboratory. The research by P.L. was supported by the Scientific Discovery through Advanced Computing (SciDAC) program funded by the US Department of Energy, Office of Science, Advanced Scientific Computing Research and Basic Energy Sciences, Division of Materials Sciences and Engineering. The work by SEN is supported by the Quantum Science Center (QSC), a National Quantum Information Science Research Center of the U.S. Department of Energy (DOE).

Appendix A: Fitting procedure

The spin wave dispersions were fitted to the data from 37 different Q vs $\hbar\omega$ slices. To avoid local minima from an over-constrained fit, we fit random subsets of the data, selecting between five and ten slices and optimizing the Hamiltonian using Scipy’s implementation of Powell’s method [48]. Then, the best fit values were accepted or rejected based on improvement of the global χ^2 (of all slices) with a simulated annealing method. This approach proved to be very effective at avoiding local χ^2 minima, which are plentiful with this data set. As a final step, we fit J_n to all slices in a steepest descent, which yielded the best fit parameters in Table I. This fitting procedure was repeated multiple times, and always converged to the same solution provided the annealing step was run for enough iterations. The code used for this fitting procedure, along with all the Gd scattering data, can be found at [insert URL]. The full set of data points used in the fitting procedure are plotted in the Supplemental Information [23].

Once the global minimum had been found, we calculated the χ^2 contour by randomly sampling points around the best fit $\{J_n\}$, and keeping those whose χ_{red}^2 was increased by less than one above the global optimum χ_{red}^2 . (This corresponds to an uncertainty of one standard deviation [49].) After a few points had been identified, we used Scikit principal component analysis [50] to identify the principal components and accompanying standard deviations in $\{J_n\}$ along which to sample, running a Monte Carlo Markov Chain (MCMC) to collect more solutions within $\Delta\chi_{red}^2 = 1$. This approach, which yielded ~ 6000 possible solutions within the $\Delta\chi_{red}^2 = 1$ contour, allows us to sample the full χ_{red}^2 landscape regardless of variation in local curvature. We take the range of possible values under the $\Delta\chi_{red}^2 = 1$ threshold, shown in Fig. 11, as an estimate of the statistical uncertainty of each fitted value.

The MCMC χ_{red}^2 sampling also reveals the correlation between different fitted parameters, as shown in Fig. 12. We quantify this by calculating a correlation matrix via Pearson correlation coefficients, which is visually plotted in Fig. 6. This reveals families of highly correlated exchange constants, especially J_3 , J_5 , J_9 , and J_{11} .

Appendix B: Origin of the anisotropic intensity at the band crossing

In this section, we explain the origin of the anisotropic neutron intensity pattern at energies above and below the K point linear band crossing. In a bipartite hexagonal lattice such as the Gd HCP structure, there are two magnon modes: the acoustic mode, where two spins in the unit cell cant the same direction; and the optical mode, where the two spins cant in opposite directions. Following the “physical picture of a spin wave” in Squires [15], they can be visualized in Fig. 13.

The neutron structure factor for magnetic correlations is

$$S^{\alpha\beta}(\mathbf{Q}, \omega) = \sum_{\ell} \int_{-\infty}^{\infty} \langle S_0^{\alpha}(0) S_{\ell}^{\beta}(t) \rangle e^{-i\mathbf{Q}\cdot\ell} e^{-i\omega t} dt, \quad (\text{B1})$$

where \sum_{ℓ} is a sum over all neighbor distances, \mathbf{Q} is the scattering vector, and $S_{\mathbf{r}}^{\beta}(t)$ is the β component of magnetization at site \mathbf{r} at time t . When \mathbf{Q} is along the $(hh0)$ direction in the bipartite hexagonal lattice, something peculiar happens: the optical magnon mode has zero intensity. This is because each $\langle S_0^{\alpha}(0) S_{\ell}^{\beta}(t) \rangle$ has a corresponding $\langle S_0^{\alpha}(0) S_{\ell}^{\beta}(t) \rangle$ of the opposite sign with the same value of $\mathbf{Q} \cdot \ell$ when \mathbf{Q} is along the $(hh0)$. This is visually clear from Fig. 13(b) and (d). Thus, when the sum \sum_{ℓ} is carried out, $S^{\alpha\beta}(\mathbf{Q}, \omega) = 0$ for the optical mode. Note that this is only true when $\mathbf{Q} = (hh0)$. As soon as \mathbf{Q} gains any orthogonal components, the optical mode gains nonzero intensity.

At the $K = (\frac{1}{3}, \frac{1}{3})$ point on the hexagonal lattice with Heisenberg exchange, the acoustic and optical magnon bands become perfectly degenerate and have a linear crossing. This is visually illustrated in Fig. 13(c)-(d), where a global rotation on a single sublattice does not change the overall system energy. Thus, at $K = (\frac{1}{3}, \frac{1}{3})$ the magnon can be rotated from zero intensity to nonzero intensity, leading to the peculiar anisotropic intensity pattern shown in panel (e). Note that this is the case for every bipartite hexagonal system, including both the 3D HCP lattice and the 2D honeycomb lattice.

This intensity pattern is observed in Gd at the K point as shown in Fig. 8, though the addition of $l = 1$ to the scattering vector inverts the argument above: because of the AB stacking in the HCP lattice, the exponential $e^{-i\mathbf{Q}\cdot\ell}$ in Eq. (B1) inverts the contribution from the other sublattice spins. This leads to the acoustic mode being invisible along $(hh1)$ and the optical mode being visible. Two other K -point linear crossings in the Gd data are shown in Figs. 14 and 15.

Appendix C: Nodal plane degeneracy

To within the instrumental resolution of this experiment, the acoustic and optical magnon modes are degenerate at half-integer ℓ in Gd. To obtain an upper bound on the Gd mode splitting—and thus on asymmetric DM interactions—we fit the scattering at $\ell = 1/2$ to a double-peak as shown in Fig. 16. Using the $(h, h, 3/2)$ line where only one mode is visible to define the resolution shape and width, we find a fitted

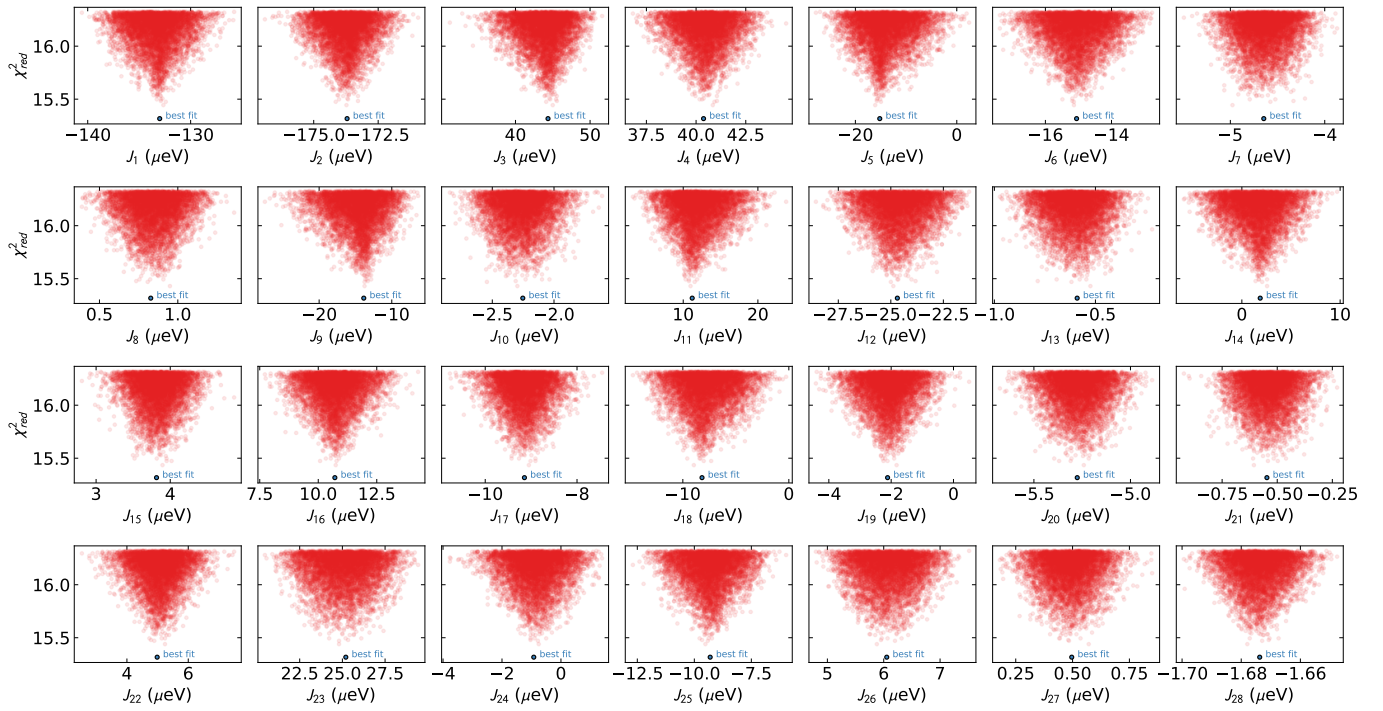


Figure 11. Possible Hamiltonian solutions within $\Delta\chi_{red}^2 = 1$ of the global optimum fit generated by MCMC. Each panel shows the range of such solutions, which we take as an estimate of uncertainty. The small blue circle represents the best fit values.

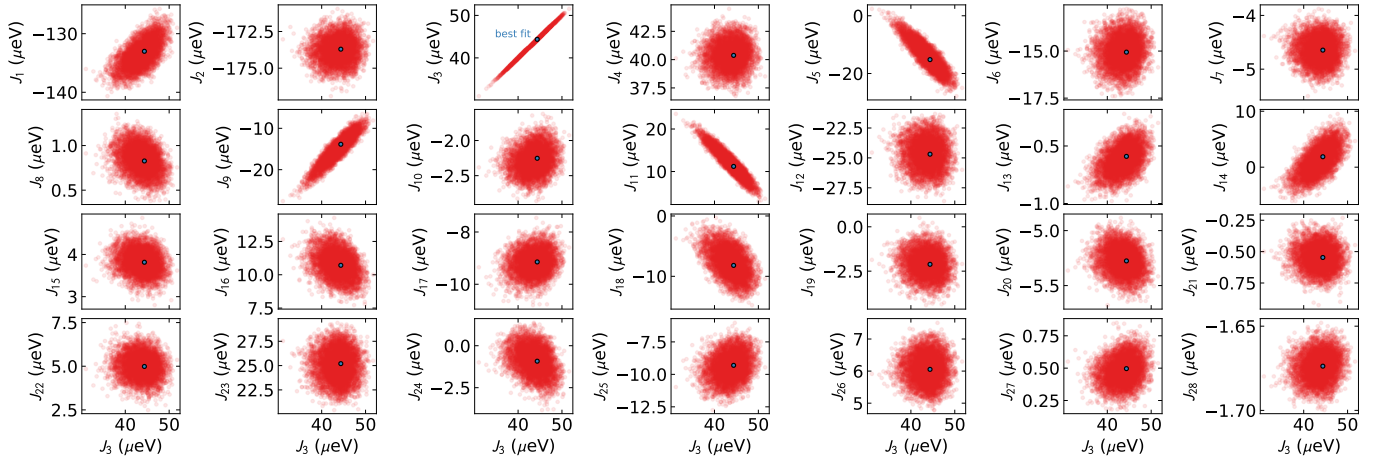


Figure 12. Hamiltonian solutions within $\Delta\chi_{red}^2 = 1$ plotted against J_3 , as an example of correlations between fitted parameters. The small blue circle represents the best fit values. A circular distribution indicates no correlation, but an ellipsoidal distribution indicates high correlation. J_5 , J_9 , and J_{11} all are highly correlated with J_3 .

maximum double-peak splitting of 0.24(5) meV, which corresponds to a maximum second neighbor DM exchange of 3(1) μ eV. Of course, the peak broadening observed in Fig. 16(b) could be from differences in resolution function be-

tween the two points—so this fit gives only an upper bound on the DM exchange interaction: at least 50 times weaker than the J_2 Heisenberg exchange interaction.

[1] G. Urbain, P. Weiss, and F. Trombe, *Comptes rendus* **200**, 2132 (1935).

[2] D. Bauer, D. Diamond, J. Li, M. McKittrick, D. Sandalow, and P. Telleen, *Critical materials strategy* (2011).

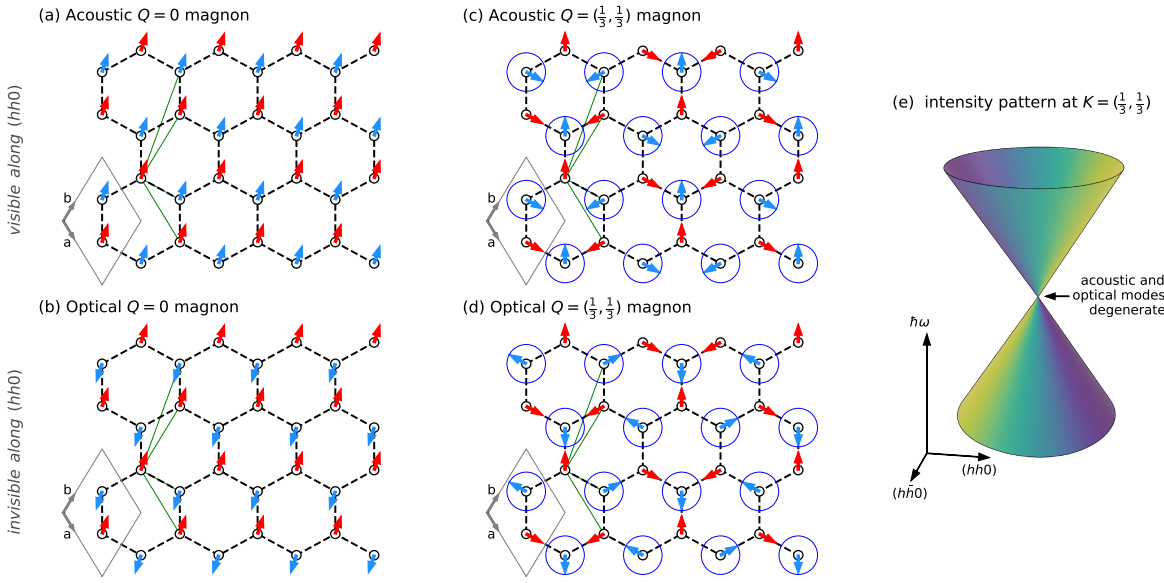


Figure 13. Origin of the anisotropic intensity around the K -point linear band crossing. Panels (a) and (b) show acoustic and optical modes of a $Q = 0$ magnon, where the arrows indicate the spin displacement from equilibrium. Panels (c) and (d) show acoustic and optical modes of a $Q = (\frac{1}{3}, \frac{1}{3})$ magnon. With only Heisenberg magnetic exchange, these two modes are related by a degenerate global rotation of a single sublattice, highlighted by the dark blue circles. The green lines indicate the ℓ in Eq. (B1) which give an equivalent $e^{-iQ\cdot\ell}$ for a neutron scattered along $(hh0)$. Because of the staggered spin displacements, the optical modes are always invisible, leading to the anisotropic intensity pattern in panel (e), where the color coding on the double cone corresponds to $S(\mathbf{Q}, \omega)$.

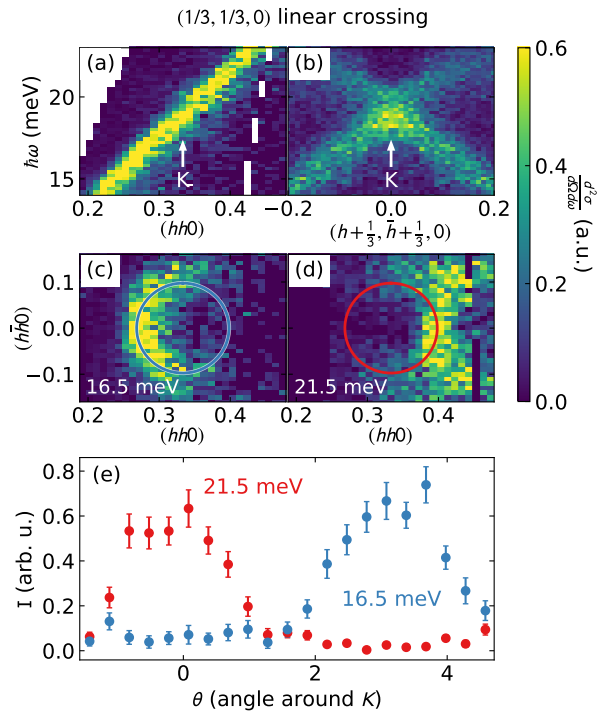


Figure 14. Linear band crossing at $K = (\frac{1}{3}, \frac{1}{3}, 0)$ measured with $E_i = 100$ meV neutrons. The resolution and statistics are notably worse than Fig. 8 with $E_i = 50$ meV, but the anisotropic intensity is still visible.

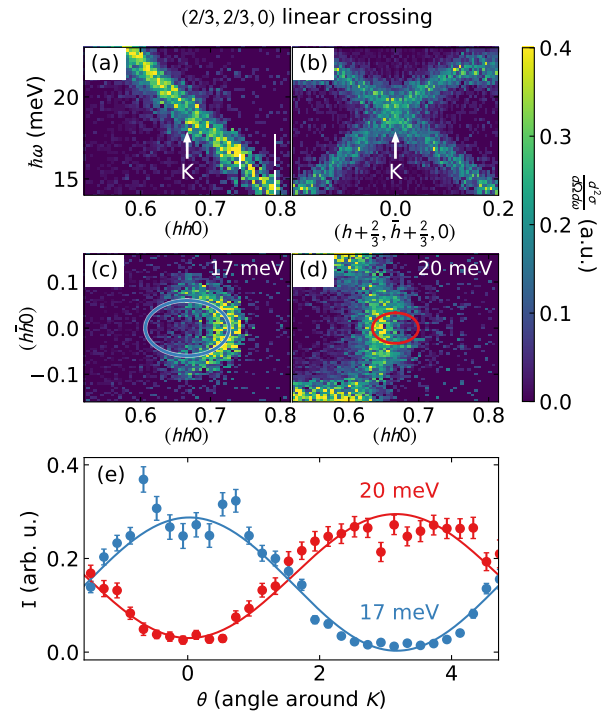


Figure 15. Linear band crossing at $K = (\frac{2}{3}, \frac{2}{3}, 0)$ measured with $E_i = 50$ meV neutrons, which again shows the anisotropic intensity pattern.

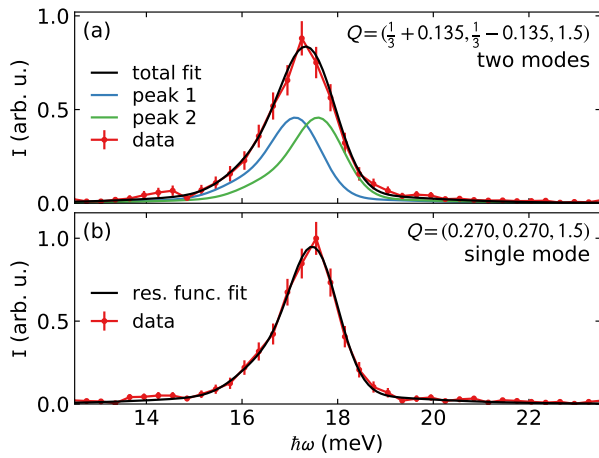


Figure 16. Mode splitting at $\ell = 3/2$ for Gd. The bottom panel shows a constant Q cut on the $(h, h, 3/2)$ line where only one mode has intensity. The top panel shows a constant Q cut near K along $(\frac{1}{3} + h, \frac{1}{3} - h, 3/2)$ where both modes have intensity. Using the bottom cut to define a resolution profile, we fit two modes of equal intensity to the top cut, yielding a maximum mode splitting of $0.24(5)$ meV—well beyond the resolution of this experiment.

- [3] D. Schüler, M. Buchert, R. Liu, S. Dittrich, and C. Merz, *Öko-Institut eV Darmstadt* **49**, 30 (2011).
- [4] J. Zhou and G. A. Fiete, *Physics Today* **73**, 10.1063/PT.3.4397 (2020).
- [5] A. Scheie, P. Laurell, G. Granroth, M. B. Stone, and S. E. Nagler, in preparation (2021).
- [6] H. E. Nigh, S. Legvold, and F. H. Spedding, *Phys. Rev.* **132**, 1092 (1963).
- [7] J. W. Cable and E. O. Wollan, *Phys. Rev.* **165**, 733 (1968).
- [8] R. M. Moon, W. C. Koehler, J. W. Cable, and H. R. Child, *Phys. Rev. B* **5**, 997 (1972).
- [9] A. F. Kip, *Rev. Mod. Phys.* **25**, 229 (1953).
- [10] J. J. M. Franse and R. Gersdorf, *Phys. Rev. Lett.* **45**, 50 (1980).
- [11] J. M. D. Coey, V. Skumryev, and K. Gallagher, *Nature* **401**, 35 (1999).
- [12] M. Colarieti-Tosti, T. Burkert, O. Eriksson, L. Nordström, and M. S. S. Brooks, *Phys. Rev. B* **72**, 094423 (2005).
- [13] S. Abdelouahed and M. Alouani, *Phys. Rev. B* **79**, 054406 (2009).
- [14] W. C. Koehler, H. R. Child, R. M. Nicklow, H. G. Smith, R. M. Moon, and J. W. Cable, *Phys. Rev. Lett.* **24**, 16 (1970).
- [15] G. L. Squires, *Introduction to the Theory of Thermal Neutron Scattering*, 3rd ed. (Cambridge University Press, Cambridge, UK, 2012).
- [16] J. Jensen and A. Mackintosh, *Rare Earth Magnetism, Structures and Excitations* (Clarendon Press, Oxford, UK, 1991).
- [17] P.-A. Lindgård, *Phys. Rev. B* **17**, 2348 (1978).
- [18] M. B. Stone, J. L. Niedziela, D. L. Abernathy, L. DeBeer-Schmitt, G. Ehlers, O. Garlea, G. E. Granroth, M. Graves-Brook, A. I. Kolesnikov, A. Podlesnyak, and B. Winn, *Review of Scientific Instruments* **85**, 045113 (2014).
- [19] G. E. Granroth, A. I. Kolesnikov, T. E. Sherline, J. P. Clancy, K. A. Ross, J. P. C. Ruff, B. D. Gaulin, and S. E. Nagler, *Journal of Physics: Conference Series* **251**, 012058 (2010).
- [20] G. E. Granroth, D. H. Vandergriff, and S. E. Nagler, *Physica B: Condensed Matter* **385-86**, 1104 (2006).
- [21] T. E. Mason, D. Abernathy, I. Anderson, J. Ankner, T. Egami, G. Ehlers, A. Ekkebus, G. Granroth, M. Hagen, K. Herwig, J. Hodges, C. Hoffmann, C. Horak, L. Horton, F. Klose, J. Laresé, A. Mesecar, D. Myles, J. Neufeind, M. Ohl, C. Tulk, X.-L. Wang, and J. Zhao, *Physica B: Condensed Matter* **385**, 955 (2006).
- [22] O. Arnold, J. Bilheux, J. Borreguero, A. Buts, S. Campbell, L. Chapon, M. Doucet, N. Draper, R. Ferraz Leal, M. Gigg, V. Lynch, A. Markvardsen, D. Mikkelsen, R. Mikkelsen, R. Miller, K. Palmen, P. Parker, G. Passos, T. Perring, P. Peterson, S. Ren, M. Reuter, A. Savici, J. Taylor, R. Taylor, R. Tolchenov, W. Zhou, and J. Zikovsky, *Nuclear Instruments and Methods in Physics Research Section A: Accelerators, Spectrometers, Detectors and Associated Equipment* **764**, 156 (2014).
- [23] See Supplemental Material at [URL will be inserted by publisher] for more details of the experiments and calculations.
- [24] P. Virtanen, R. Gommers, T. E. Oliphant, M. Haberland, T. Reddy, D. Cournapeau, E. Burovski, P. Peterson, W. Weckesser, J. Bright, *et al.*, *Nature Methods* **17**, 261 (2020).
- [25] J. W. Cable, N. Wakabayashi, and R. M. Nicklow, *Journal of Applied Physics* **52**, 2231 (1981).
- [26] J. W. Cable, R. M. Nicklow, and N. Wakabayashi, *Phys. Rev. B* **32**, 1710 (1985).
- [27] J. W. Cable and R. M. Nicklow, *Phys. Rev. B* **39**, 11732 (1989).
- [28] M. A. Ruderman and C. Kittel, *Phys. Rev.* **96**, 99 (1954).
- [29] T. Kasuya, *Progress of Theoretical Physics* **16**, 45 (1956).
- [30] K. Yosida, *Phys. Rev.* **106**, 893 (1957).
- [31] P. G. Mattocks and R. C. Young, *Journal of Physics F: Metal Physics* **7**, 1219 (1977).
- [32] I. Turek, J. Kudrnovsk, G. Bihlmayer, and S. Blügel, *Journal of Physics: Condensed Matter* **15**, 2771 (2003).
- [33] A. T. Hindmarch and B. J. Hickey, *Phys. Rev. Lett.* **91**, 116601 (2003).
- [34] R. E. Watson and A. J. Freeman, *Phys. Rev.* **178**, 725 (1969).
- [35] P. A. Lindgård, B. N. Harmon, and A. J. Freeman, *Phys. Rev. Lett.* **35**, 383 (1975).
- [36] W. Brinkman, *Journal of Applied Physics* **38**, 939 (1967).
- [37] A. P. Cracknell, *J. Phys. C: Solid State Phys.* **3**, S175 (1970).
- [38] P. McClarty, *arXiv preprint arXiv:2106.01430* (2021).
- [39] P. A. McClarty and J. G. Rau, *Phys. Rev. B* **100**, 100405 (2019).
- [40] S. Shivam, R. Coldea, R. Moessner, and P. McClarty, *arXiv preprint arXiv:1712.08535* (2017).
- [41] T. Moriya, *Phys. Rev.* **120**, 91 (1960).
- [42] S. Toth and B. Lake, *Journal of Physics: Condensed Matter* **27**, 166002 (2015).
- [43] R. M. Nicklow, N. Wakabayashi, M. K. Wilkinson, and R. E. Reed, *Phys. Rev. Lett.* **26**, 140 (1971).
- [44] H. B. Möller, J. C. G. Houmann, and A. R. Mackintosh, *Journal of Applied Physics* **39**, 807 (1968).
- [45] T. Perring, A. Taylor, and G. Squires, *Physica B: Condensed Matter* **213**, 348 (1995).
- [46] O. W. Dietrich and J. Als-Nielsen, *Phys. Rev.* **162**, 315 (1967).
- [47] L. W. Roeland and G. J. Cock, *Journal of Physics C: Solid State Physics* **8**, 3427 (1975).
- [48] M. J. D. Powell, *The Computer Journal* **7**, 155 (1964).
- [49] W. H. Press, S. A. Teukolsky, W. T. Vetterling, and B. P. Flannery, *Numerical recipes 3rd edition: The art of scientific computing* (Cambridge university press, 2007).
- [50] F. Pedregosa, G. Varoquaux, A. Gramfort, V. Michel, B. Thirion, O. Grisel, M. Blondel, P. Prettenhofer, R. Weiss, V. Dubourg, J. Vanderplas, A. Passos, D. Cournapeau, M. Brucher, M. Perrot, and Édouard Duchesnay, *Journal of Machine Learning Research* **12**, 2825 (2011).